

Diagrammatic exciton-basis valence-bond theory of linear polyenes

M. Chandross

SPAWAR Systems Center, Code D364, San Diego, California 92152

Y. Shimoi

Electrotechnical Laboratory, 1-1-4 Umezono, Tsukuba 305, Japan

S. Mazumdar

*Department of Physics, University of Arizona, Tucson, Arizona 85721
and The Optical Sciences Center, University of Arizona, Tucson, Arizona 85721*

(Received 10 August 1998)

Understanding the photophysics of π -conjugated polymers requires a physical understanding of the excited states involved in the photophysics. Detailed physical understanding is difficult because of the extensive configuration interaction that occurs within realistic theoretical models for these systems. We develop a diagrammatic exciton-basis valence-bond representation that is particularly suitable for the intermediate magnitude of the Coulomb interactions in these systems. We present detailed comparisons of our exact exciton-basis treatment and previous approximate approaches, focusing on the specific many-body and single-particle interactions that have been ignored in the past, and the consequences thereof. Following this, we present the results of exact numerical calculations for the noninteracting band limit, the limit of isolated dimers interacting through Coulomb interactions, and for the Pariser-Parr-Pople Ohno Coulomb interactions with two different bond-alternation parameters for the ten-carbon linear polyene. Simple pictorial descriptions of the eigenstates relevant in photophysics are obtained in each case, and taken together, these results provide a systematic characterization of both low- and high-energy excited states in linear chain π -conjugated systems for realistic parameters. Two different quantities, the number of effective excitations within the exciton basis, and the particle-hole correlation length for the one-excitation eigenstates are defined and calculated for further quantitative comparisons between the eigenstates. A pictorial description of optical nonlinearity is obtained thereby. For both small and large bond alternation, it is found that the two-photon state that dominates third order optical nonlinearity in the low-energy region is the lowest even parity one-excitation state with a larger particle-hole correlation length than the $1B_u$ exciton. The reason for the dominance by this mA_g state can be understood within the exciton basis from the nature of the current operator. It is shown that the relationship between the correlated mA_g and the correlated $1B_u$ is identical to that between the uncorrelated $2A_g$ and the uncorrelated $1B_u$. In the high-energy region of the spectrum evidence for stable biexcitons is found from the nature of the singlet-singlet two-excitation wave functions. [S0163-1829(99)01408-3]

I. INTRODUCTION

The effect of electron-electron interactions on the energy spectra of π -conjugated polymers continues to be a topic of current interest.^{1,2} Recent discussions in this area have largely centered on the band versus exciton character of the lowest optical state, and the associated effects on the photophysics of the experimental systems.^{3,4} Although there is now a broad consensus that the optical $1B_u$ state in π -conjugated polymers is an exciton, there is no general agreement on the magnitude of the exciton binding energy, as well as excitonic effects on the photophysics. The primary reason for this is that electron-electron interactions in the experimental systems are intermediate in magnitude, with the on-site Coulomb interaction (the Hubbard interaction) being close to four times the one-electron hopping integral between neighboring carbon atoms.^{5,6} Direct theoretical determinations of exciton binding energies and excitonic effects on the photophysics then are difficult, because of the many-body nature of the Coulomb-correlated π -electron Hamiltonian.

Theoretical approaches to understanding the excited state energy spectra of π -conjugated polymers have in many cases focused on the available nonresonant and resonant nonlinear spectroscopic experimental results.⁷⁻¹⁴ Broadly speaking, these approaches can be classified as (a) approximate long-chain calculations that include the configuration interaction (CI) among a subset of the one-electron configurations,¹⁵⁻¹⁷ and (b) exact, or full configuration-interaction (FCI) calculations for short chains¹⁸⁻²³ (we do not attempt to make finer distinctions between the FCI calculations and the multireference double-CI calculations of Beljonne *et al.*,²⁴ which incorporate the most important high-order CI terms. The chain lengths reached by this method are roughly about twice that of the FCI calculations, and the advantages as well as disadvantages of this technique are comparable to those of the FCI calculations). The approximate calculations miss the low energy even parity A_g states that occur below the $1B_u$ state in linear polyenes²⁵ as well as any possible biexciton states. Furthermore, within these approaches the energy of the conduction-band threshold (the Hartree-Fock band gap) is independent of the Hubbard interaction. This result is clearly

incorrect. On the other hand, although short-chain calculations can give the correct ordering of excited states in the low-energy region, the energies of excited states found to be important in nonlinear optics in these calculations are still very far from their long-chain limiting values. As a consequence, there exist fundamental disagreements over the interpretations of the physical natures and energy locations of the excited states that dominate nonlinear spectroscopy.^{26,27} Very recently, the density-matrix renormalization group²⁸ (DMRG) approach has been used to understand some of the same excited eigenstates. At the moment, however, several of the DMRG results, as obtained by different practicing groups^{29–31} seem to be different in their detailed predictions, and further progress in this promising area would be necessary before definitive conclusions are reached. Furthermore, it has until now not been possible to probe excited states that are near twice the energy of the $1B_u$ (Refs. 21 and 32) using the DMRG approach (see, however, note added at the end of the paper).

In the present paper, we report a new approach to exact short-chain calculations that focuses on the *wave functions*, rather than energetics. The goal of this work is to develop a pictorial, physical characterization of excited states, in particular, those eigenstates that are most relevant to the photo-physics. Although the FCI nature of our calculations limits us to short chains, we believe that by focusing on the wave functions we can bypass the disadvantages usually associated with short-chain calculations. As we discuss here, whether a particular eigenstate evolves into a localized exciton or delocalized bandlike state as the chain length is progressively increased can be determined by careful inspection of the eigenstate in question, provided the right basis space is used. This is particularly true if proper care is exercised in comparing the eigenstates of the full Pariser-Parr-Pople (PPP) Hamiltonian^{5,6} with those of limiting band and localized models, whose eigenstates are already understood physically. This is precisely the approach taken here. One argument that can be given against such short-chain calculations is that because of confinement effects associated with short chains, excitonic effects are exaggerated in short chain calculations (since, for example, there always is an energy gap between the optical $1B_u$ and higher excited states in short chains). We do not believe this to be a serious problem. A recent work has shown that although exciton formation is conditional when only nearest-neighbor intersite Coulomb interaction is retained, the optical state is necessarily an exciton when the intersite Coulomb interactions are long range,³³ as indeed they are within the PPP model.^{5,6}

The intermediate magnitude of the Coulomb interactions in π -conjugated systems implies that standard CI calculations are not suitable for the physical interpretation of eigenstates that is our goal. For PPP interactions, even in short chains, extensive configuration interaction occurs among the fundamental one-electron molecular orbital (MO) basis functions. As a consequence, a given excited state eigenstate is a superposition of numerous MO configurations, such that the simple physical picture that describes the band limit of zero Coulomb interactions is lost entirely. This is particularly true for high-energy excited states that occur considerably above the $1B_u$ exciton. An alternate approach to CI, using configuration space valence-bond (VB) basis functions, has been

used by Soos and coworkers^{2,34,35} to understand the physical characteristics of the lowest eigenstates for realistic Coulomb correlations, and by us for understanding nonlinear spectroscopy in the limit of infinite on-site Coulomb interaction.^{19,21} High-energy excited states for realistic Coulomb interactions are very complex even within the standard VB approach, once again, precisely for the reason that such eigenstates are superpositions of many simple VB diagrams. On the other hand, the *requirement* for a theory within which simple physical characterization of eigenstates could be obtained, is clear from both the MO and VB approaches to CI. Specifically, eigenstates should be superpositions of a *few* dominant basis functions that are themselves easy to interpret physically. This is the logic that has gone into our development of the diagrammatic exciton-basis VB approach to eigenstates of the PPP model. The basis states here are *hybrids* of MO and configuration space VB functions, and are therefore ideal for the case of intermediate Coulomb interactions. A brief presentation of the diagrammatic exciton-basis method has been made previously.³⁶ We give here a complete discussion of the transformation of the Hamiltonian to the exciton space, physical interpretations of the eigenstates in simple limiting cases as well as in realistic cases and a pictorial interpretation of nonlinear absorption. Although our focus is on the PPP interactions, we also present a brief discussion of the evolution of the eigenstates as the Coulomb interactions are varied from weak to strong.

The exciton-basis VB approach that we present here is an extension of the molecular exciton approach to linear polyenes, as originally formulated by Simpson,³⁷ within which a linear polyene is visualized as coupled ethylenic two-level units. Within the original Simpson approach, there is no electron-hole delocalization between the units, and optical excitation is to a tightly-bound Frenkel exciton, which can, however, form an exciton band due to exciton migration. Furthermore, all interunit many-body interactions between the dimeric units are neglected. Unless electron-hole delocalization between the units and the many-body Coulomb interactions are incorporated, the Simpson model can apply only to molecular aggregates.^{38,39} Over the years, different investigators have gone beyond the simplest exciton picture to describe real π -conjugated systems.^{40–48} However, as we discuss later, in nearly all of these cases important one-electron as well as many-body interactions that occur in the standard Pariser-Parr-Pople (PPP) Hamiltonian^{5,6} for conjugated systems were ignored. As a consequence, the results obtained within these approaches are of limited value (see below). The two exceptions to this are the works by Ohmine *et al.*⁴² and Mukhopadhyay *et al.*⁴⁶ Ohmine *et al.* carried out a singles-CI calculation of long polyene systems within the exciton approach, without ignoring any term in the PPP model. Because of the neglect of higher order CI, however, accurate results for the even parity A_g states could not be obtained. In contrast, Mukhopadhyay *et al.* carried out their FCI calculations using the configuration space VB approach in the limit of artificially large bond alternation, and calculated overlaps with the simplest basis functions within the exciton representation. This approach cannot be extended to the case of realistic bond alternation, where there is considerable configuration mixing. The resultant physical descrip-

tion, while still of value, is thus not applicable to the case of realistic polyenes.

In contrast to the earlier work,^{40–45,47,48} the present calculations using the exciton-basis VB diagrams are exact. We retain all terms within the full PPP Hamiltonian, and our calculations are then carried out using the exciton representation directly. There is, however, a price to pay. Because of the FCI nature of our calculations, they are necessarily limited to short chains (specifically, to the case of the 10-carbon chain). Since our aim, however, is to obtain benchmark *qualitative* results that provide physical insight, and against which approximate long-chain calculations (including the DMRG approach) can be tested in the future, we believe that this is a small price to pay. This is especially because our focus is on wave functions, and not on energies. As we show here, even though the energies of the short-chain polyenes are very far from their infinite chain values, the physical natures of the various *classes* of wave functions (viz., localized exciton states, delocalized bandlike states, biexciton states, etc.) are already visible at short chain lengths within the diagrammatic exciton-basis VB theory.

In Sec. II we present a complete discussion of the basis space and the transformation of the PPP Hamiltonian into a form that is suitable for direct calculations of exact eigenstates using the exciton-basis VB diagrams. The specific terms that have been neglected in the past within the approximate exciton-basis calculations^{40,43–45,47,48} and their importance are discussed. In Sec. III, we present the relevant results for the two limiting cases of the simple one-electron Hückel model for polyenes and for the case of PPP Coulomb interactions with zero interunit electron-transfer. The second scenario is related, but is not identical to, model Hamiltonians that are used to discuss molecular aggregates.^{38,39} Our goal is to obtain a complete picture of the evolution of the eigenstates as various interactions are incorporated, and these two limiting cases serve very well towards that purpose. In Sec. IV, we discuss the complete PPP model, for two different bond alternation parameters, corresponding to the cases of linear polyenes and polysilanes. The physical insight that is obtained for the wave functions relevant in the photophysics here leads directly to a qualitative picture of the dominant nonlinear optical channels, as is shown in Sec. V. In Sec. VI, we discuss the evolution of wave functions as a function of the strength of the Coulomb parameters. The conclusion that emerges from our work is that *provided the intersite Coulomb interactions are strong enough to give excitons*, the relationship between the optically relevant eigenstates as well as the dominant nonlinear optical channels are almost independent of the actual magnitudes of the Coulomb parameters. Only the actual configurations that describe a particular wave-function change continuously as the overall wave function evolves, but this is to be expected.

II. THE PPP HAMILTONIAN AND THE EXCITON BASIS

We discuss in this section the construction of the exciton-basis valence-bond (VB) diagrams, and the transformation of the PPP Hamiltonian from the atomic representation into the exciton representation.

A. The atomic basis

The PPP model is commonly written within the atomic representation

$$H = - \sum_{\langle ij \rangle, \sigma} t_{ij} (c_{i\sigma}^\dagger c_{j\sigma} + c_{j\sigma}^\dagger c_{i\sigma}) + U \sum_i n_{i\uparrow} n_{i\downarrow} + \sum_{i < j} V_{ij} (n_i - 1)(n_j - 1), \quad (1)$$

where $\langle \rangle$ implies nearest neighbors, $c_{i\sigma}^\dagger$ creates an electron of spin σ on the p_z orbital of carbon atom i , $n_{i\sigma} = c_{i\sigma}^\dagger c_{i\sigma}$ is the number of electrons with spin σ on atom i , and $n_i = \sum_\sigma n_{i\sigma}$ is the total number of electrons on atom i . The parameters U and V_{ij} are the on-site and long-range Coulomb interactions, respectively, while t_{ij} is the one-electron hopping matrix element. In the case of linear polyenes and polyacetylenes, $t_{ij} = t(1 \pm \delta)$ where δ is a rigid bond alternation parameter. Within the Ohno parameterization of the PPP Hamiltonian,⁴⁹ $t = 2.4$ eV, $U = 11.13$ eV, and the V_{ij} are obtained from the relationship

$$V_{ij} = \frac{U}{\sqrt{1 + 0.6117R_{ij}^2}}, \quad (2)$$

where R_{ij} is the distance in Å between carbon atoms i and j .

B. Exciton-basis VB diagrams

We begin by transforming the site operators in Eq. (1) to the creation and annihilation operators for the ethylenic bonding and antibonding MO's,

$$a_{i,\lambda,\sigma}^\dagger = \frac{1}{\sqrt{2}} [c_{2i-1,\sigma}^\dagger + (-1)^{(\lambda-1)} c_{2i,\sigma}^\dagger], \quad (3)$$

$$a_{i,\lambda,\sigma} = \frac{1}{\sqrt{2}} [c_{2i-1,\sigma} + (-1)^{(\lambda-1)} c_{2i,\sigma}], \quad (4)$$

where $a_{i,\lambda,\sigma}^\dagger$ ($a_{i,\lambda,\sigma}$) creates (annihilates) an electron of spin σ in the bonding ($\lambda = 1$) or antibonding ($\lambda = 2$) MO of ethylene unit i . Many-electron configurations are then of the form $\prod_{i,\lambda,\sigma} a_{i,\lambda,\sigma}^\dagger |0\rangle$, where $|0\rangle$ is the vacuum. Instead of working directly with this particular representation, we construct VB diagrams that are linear combinations of the many-electron exciton-basis configurations, as the VB representation allows block diagonalization of the Hamiltonian into different total spin S subspaces.

The VB exciton basis is best understood from illustration. We therefore begin with a description of the simplest building blocks of the correlated wave functions of long chains within the VB exciton basis. The VB exciton bases for ethylene are trivial, and consist of only three diagrams, (i) doubly occupied bonding MO, empty antibonding MO, (ii) singly occupied bonding MO, singly occupied antibonding MO, and (iii) doubly occupied antibonding MO, empty bonding MO. The complications encountered in the many-unit case are first encountered in the case of the two-unit case (butadiene). We illustrate the exciton basis by discussing the exciton-basis VB diagrams for the two-unit case in detail.

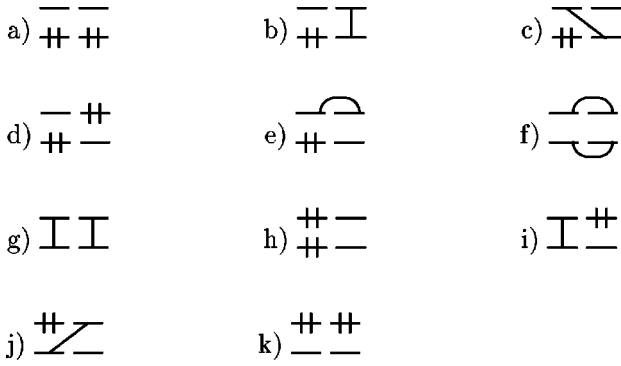


FIG. 1. Exciton-basis diagrams for $N=2$. Bonding and antibonding MO's of the coupled two-level systems are occupied by 0, 1, and 2 electrons. Singly occupied MO's are paired as singlet bonds. Mirror-plane and charge-conjugation symmetries are assumed (see text).

In Fig. 1 we show the VB exciton diagrams for the simple two-unit oligomer. The diagram (a) in Fig. 1 is the product wave function of the ground states of two noninteracting units, which we refer to hereafter as the Simpson ground state. All other VB exciton diagrams are one-, two-, . . . $2N$ -electron excitations from the Simpson ground state of a N -unit chain. In our description of eigenstates we will go back and forth between CI theory involving MO basis functions and the exciton-basis VB diagrams. In order to distinguish between MO and exciton-VB configurations we will use the following nomenclature. MO configurations excited from the Hückel ground state will be referred to as $ne-nh$ (for n electron- n hole excitations), while exciton-VB diagrams will be described as n excitations. With this nomenclature in place, we now describe the remaining basis functions in Fig. 1 below. A bond connecting two MO's i and j is the spin-singlet linear combination $2^{-1/2}(a_{i,\lambda,\uparrow}^\dagger a_{j,\lambda',\downarrow}^\dagger - a_{i,\lambda,\downarrow}^\dagger a_{j,\lambda',\uparrow}^\dagger)|0\rangle$, as in configuration space VB theory. The intraunit excitation in diagram (b) and the interunit excitation in diagram (c) are both singly excited with respect to the Simpson ground state (a). All diagrams of the type (c), in which charge transfer from one unit to another has occurred, are hereafter referred to as CT. Although for both (b) and (c) we show a single diagram, mirror-plane symmetry is assumed and each diagram also represents the diagram that would be obtained by reflection about the symmetry plane passing through the center of the chain. In addition to mirror-plane symmetry, diagrams in the exciton basis may be related by charge-conjugation symmetry,⁵⁰ in which double occupancies and vacancies are interchanged. As an example, in Fig. 2 we show the complete A_g basis state (i.e., with all symmetry related diagrams) corresponding to diagram (e) in Fig. 1 [see below for more discussion of diagram (e)]. The “plus” linear combination of diagram (b) and its mirror-plane counterpart occurs only in the optical B_u subspace,

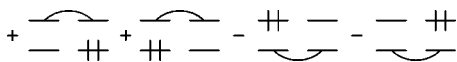


FIG. 2. Linear combination of exciton-basis VB diagrams that are related by mirror-plane and charge-conjugation symmetry. The particular linear combination shown forms a single basis function in the A_g subspace.

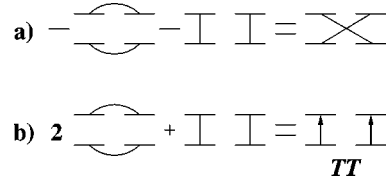


FIG. 3. Linear combination of exciton-basis VB diagrams that give a (a) crossed diagram, and (b) a TT diagram.

while linear combinations of (c) and its reflected version occur in both the A_g and B_u subspaces.

The next group of diagrams in Fig. 1, (d) through (h), consist of two excitations from the Simpson ground state (a). Diagram (d) has one doubly excited unit, while diagram (e) involves both two excitation and CT. CT between the bonding MO's couples (e) and (f). Note that (f) is distinct from (g), although the orbital occupancies of (f) and (g) are the same. The diagrams beyond (g) in Fig. 1 have little relevance in the physical descriptions of optical processes, although their inclusion in calculations is important for accurate energies and wave functions.

Before proceeding further we note three interesting features of diagrams (f) and (g) in Fig. 1. First, the two diagrams are not orthogonal, and the corresponding overlap integral $\langle f|g\rangle = -1/2$. Second, the linear combination $-|f\rangle - |g\rangle$ is equivalent to a “crossed” diagram, in which the bonding (antibonding) MO of a given unit is bonded to the antibonding(bonding) MO of a neighboring unit [see Fig. 3(a)]. This diagram will be relevant in the context of biexciton wave functions with large bond alternation. The third interesting feature of these diagrams is that the linear combination $2|f\rangle + |g\rangle = TT$, where TT implies a pair of triplet ($S=1$) excitations localized on different units that are coupled to form an overall spin singlet [see Fig. 3(b)],

$$TT = - \sum_{\sigma} a_{i,1,\sigma}^\dagger a_{i,2,\sigma}^\dagger a_{j,1,-\sigma}^\dagger a_{j,2,-\sigma}^\dagger + \frac{1}{\sqrt{2}} \times (a_{i,1,\uparrow}^\dagger a_{i,2,\downarrow}^\dagger + a_{i,1,\downarrow}^\dagger a_{i,2,\uparrow}^\dagger) \frac{1}{\sqrt{2}} (a_{j,1,\uparrow}^\dagger a_{j,2,\downarrow}^\dagger + a_{j,1,\downarrow}^\dagger a_{j,2,\uparrow}^\dagger). \quad (5)$$

Equation (5) can be proved by simply writing out the formal expression for diagrams (f) and (g). There are three distinct terms in Eq. (5). These correspond to $(S_z^i, S_z^j) = (+1, -1); (-1, +1);$ and $(0, 0)$ excitations on the individual units, where S_z^i is the z component of the spin on unit i .

The exciton-basis VB diagrams for chains longer than two units are similarly obtained by considering all possible excitations out of the corresponding Simpson ground state, and constructing the appropriate singlet linear combinations. The possibility of multiple excitations out of the Simpson ground state introduces only two qualitatively new features. Firstly, multiple electron-hole excitations in long chains can lead to diagrams of the type $TTT, TTTT,$ etc., which like the TT diagrams consist of multiple intraunit triplet excitations that combine to give an overall singlet.⁴⁶ An example of a TTT diagram for the three-unit case is shown in Fig. 4(a). Sec-

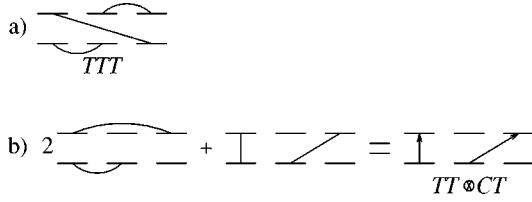


FIG. 4. (a) A TTT exciton-basis VB diagram, (b) linear combination of exciton-basis VB diagrams corresponding to $TT \otimes CT$.

only, more complicated versions of the 2:1 linear combination of the type in Fig. 3(b) are now possible, as is shown in Fig. 4(b). As in the case of Fig. 3, it is easily proved by writing out the formal expressions for the two diagrams on the left that the 2:1 combination is equivalent to two triplets, which however, are no longer localized on individual units. We shall refer to this combination as $TT \otimes CT$.

C. Transformation of the PPP Hamiltonian

We now show the complete transformation of the PPP Hamiltonian into the exciton basis, using the operators in Eqs. 3 and 4. We rewrite the PPP Hamiltonian in the following form:

$$H = H_{intra}^{CT} + H_{inter}^{CT} + H_{ee} \quad (6)$$

$$H_{ee} = H_U + H_V. \quad (7)$$

In Eq. (6), H_{intra}^{CT} and H_{inter}^{CT} describe the one-electron charge transfer within and between neighboring ethylene units, respectively, and H_{ee} contains the terms describing the Coulomb interactions among the π electrons.

The intraunit charge-transfer H_{intra}^{CT} is written as

$$H_{intra}^{CT} = -t_1 \sum_{i\sigma} (c_{2i-1,\sigma}^\dagger c_{2i,\sigma} + c_{2i,\sigma}^\dagger c_{2i-1,\sigma}). \quad (8)$$

In the above, $t_1 = t(1 + \delta)$ is the matrix element corresponding to the hopping of electrons within a dimeric unit. For a chain with $2N$ carbon atoms, H_{intra}^{CT} describes N uncoupled two-level systems, and the solutions of H_{intra}^{CT} are the N -fold degenerate bonding and antibonding MO's of a single ethylenic unit. H_{intra}^{CT} is diagonal within this representation.

$$H_{intra}^{CT} = -t_1 \sum_{i,\lambda,\sigma} (-1)^{(\lambda-1)} a_{i,\lambda,\sigma}^\dagger a_{i,\lambda,\sigma}. \quad (9)$$

The remaining terms of the PPP Hamiltonian are now written in terms of the exciton-basis operators. The interunit charge-transfer term is given by

$$H_{inter}^{CT} = -\frac{1}{2} t_2 \sum_{i,\lambda,\lambda',\sigma} (-1)^{(\lambda-1)} \times [a_{i,\lambda,\sigma}^\dagger a_{i+1,\lambda',\sigma} + a_{i+1,\lambda',\sigma}^\dagger a_{i,\lambda,\sigma}], \quad (10)$$

where $t_2 = t(1 - \delta)$ is the hopping matrix element between dimer units. Note that H_{inter}^{CT} contains three kinds of terms, which correspond to electron transfer between (i) the bonding MO's of neighboring units ($\lambda = \lambda' = 1$), (ii) the antibonding MO's of neighboring units ($\lambda = \lambda' = 2$), and (iii)

between the bonding MO of one unit and the antibonding MO of a neighboring unit ($\lambda \neq \lambda'$). With our phase convention for the exciton-basis operators [Eqs. (3) and (4)], the matrix element corresponding to the CT between the antibonding MO of the i th unit and either MO of the $(i+1)$ th unit is negative, although the magnitudes of all CT matrix elements are the same.

The on-site Coulomb interaction is written as

$$H_U = \frac{U}{2} \left[\sum_{i,\lambda,\lambda'} N_{i,\lambda,\uparrow} N_{i,\lambda',\downarrow} + \sum_i \sum_{\lambda_1 \neq \lambda_2} \sum_{\lambda_3 \neq \lambda_4} a_{i,\lambda_1,\uparrow}^\dagger a_{i,\lambda_2,\uparrow} a_{i,\lambda_3,\downarrow}^\dagger a_{i,\lambda_4,\downarrow} \right]. \quad (11)$$

In the above, $N_{i,\lambda,\sigma} = a_{i,\lambda,\sigma}^\dagger a_{i,\lambda,\sigma}$ is the occupation within MO λ of the i th unit. This term contains both density-density correlations and two electron hops involving MO's within a unit.

The intersite electron-electron interaction is more complicated than the on-site term, and is written as

$$H_V = \frac{1}{2} \sum_{i,j} \sum_{m,n} V_{ijmn} (v_{i,m} - 1)(v_{j,n} - 1), \quad (12)$$

where $v_{i,m}$ is the number of electrons on the m th atom ($m = 1, 2$) of the i th dimer unit, and is given by

$$v_{i,m} = \sum_{\sigma,\lambda} \sum_{\lambda_1 \neq \lambda_2} \frac{1}{2} [N_{i,\lambda,\sigma} - (-1)^m a_{i,\lambda_1,\sigma}^\dagger a_{i,\lambda_2,\sigma}], \quad (13)$$

and V_{ijmn} is the Ohno potential between atom m on unit i and atom n on unit j . From Eqs. (12) and (13), H_V contains three kinds of terms: density-density correlations, two-electron hops, and products of density and electron hopping between MO's.

As discussed above, several groups have obtained limited results within simplified exciton-basis Hamiltonians.^{43-45,47,48} Within these simplified models the electron hopping between the bonding MO of one unit and the antibonding MO of a neighboring unit in H_{inter}^{CT} ($\lambda \neq \lambda'$ in Eq. 10) is ignored. Furthermore, only the density-density correlation terms within H_U and H_V are retained, and terms containing two-electron hops and products of density and electron hop are discarded. Within these approximations the number of excitations from the Simpson ground state becomes a true quantum number. The ground state within the simplified models^{43-45,47,48} is therefore the Simpson ground state. Similarly, all one excitations are completely decoupled from two excitations, which are again decoupled from higher excitations, and so on. Although such block diagonalizations make numerical simulations of relatively long chains possible [and even analytic results can be obtained in the limit of $H_V = 0$ (Refs. 40 and 47)], such simplification is achieved at the cost of ignoring terms in the PPP Hamiltonian that are of comparable magnitude to those that are retained. Important low-lying correlated states (for example, the true $2A_g$ state) are therefore missed within such calculations. Furthermore, as we discuss later, the description of the true biexciton state is different from that obtained within the simple models.

Since our primary concern is the description of states reached by linear and nonlinear optical excitations, we also transform the dipole operator to the exciton basis. In the atomic representation, the dipole operator is

$$\hat{\mu} = \sum_i n_i x_i, \quad (14)$$

where x_i is the position of atom i . In Eq. (14), we have taken the electronic charge as well as the lattice spacing to be 1 for simplicity. Previous work has shown that for the Ohno parameterization differences in dipole couplings that arise from explicitly including the bond alternation in the expression for $\hat{\mu}$ is tiny (bond alternation can lead to large differences in dipole moments, but this is a consequence of the different natures of the eigenstates of the dimerized Hamiltonian, and not of modifying $\hat{\mu}$).^{34,35} Within the exciton basis, the dipole operator is transformed to

$$\hat{\mu} = \sum_{i,\lambda,\sigma} (2N - 4i + 2) N_{i,\lambda,\sigma} + \sum_{i,\sigma} \sum_{\lambda_1 \neq \lambda_2} a_{i,\lambda_1,\sigma}^\dagger a_{i,\lambda_2,\sigma}, \quad (15)$$

where $2N$ is the total chain length. For a physical picture of the couplings introduced by optical excitation between eigenstates, it is also useful to discuss the current operator $\hat{j} = i[H, \hat{\mu}]$, where H is the Hamiltonian and $[\dots]$ is the commutator. Within the atomic basis \hat{j} is given by

$$\hat{j} = i \sum_i t_{i,i+1} (x_{i+1} - x_i) (c_{i,\sigma}^\dagger c_{i+1,\sigma} - c_{i+1,\sigma}^\dagger c_{i,\sigma}). \quad (16)$$

Within the exciton basis, this is transformed to the following expression:

$$\begin{aligned} \hat{j} = & i t_1 \sum_{i,\sigma} (a_{i,2,\sigma}^\dagger a_{i,1,\sigma} - a_{i,1,\sigma}^\dagger a_{i,2,\sigma}) \\ & - i (t_2/2) \sum_{i,\sigma} \sum_{\lambda,\lambda'} (a_{i,\lambda,\sigma}^\dagger a_{i+1,\lambda',\sigma} - a_{i+1,\lambda',\sigma}^\dagger a_{i,\lambda,\sigma}). \end{aligned} \quad (17)$$

From the commutation relationship between the dipole and the current operators, one further obtains the following relationship:⁵¹

$$\langle \Psi_a | \hat{\mu} | \Psi_b \rangle = \frac{1}{\Delta E} \langle \Psi_a | \hat{j} | \Psi_b \rangle, \quad (18)$$

where ΔE is the energy difference between the eigenstates. From Eq. (17), the current operator induces electron transfers between the bonding or antibonding MO's of neighboring units. From Eq. (18), transition dipole moments are largest when the transfers induced by the current operator are between neighboring MO's with the *same* λ . For transfers between $\lambda \neq \lambda'$, ΔE is larger, and the dipole coupling is smaller. This concept will be very useful in understanding the large differences in transition dipole couplings between excited eigenstates of the PPP model (see below).

We now proceed to the results of calculations within the exciton basis. Our calculations are for $N = 5$, for which we construct and solve exactly the full CI matrices for the A_g

and B_u subspaces. The physical natures of the optically relevant eigenstates are then discussed in terms of the dominant exciton-basis VB diagrams. We will begin with results from the Hückel model, which includes hopping between the dimer units, but sets all electron-electron interactions to zero. Following this, we will present results from the opposite limit, in which interunit hopping is disallowed, but the full electron-electron interactions are retained. These two complementary limiting cases will make the results of calculations within the full Hamiltonian (i.e., with full interdimer hopping and electron-electron interactions) easier to understand and interpret. Due to the excessively large number of eigenfunctions of the full PPP Hamiltonian, we will be restricting our discussions to those states that are relevant to the nonlinear optical properties of conjugated systems. These states are the $1A_g$ ground state, the $1B_u$ optical state, and the even-parity mA_g state(s) most strongly coupled to the $1B_u$.¹⁵⁻²³ We will additionally discuss the low-energy TT states, as well as the higher energy bound and free two-exciton states in the correlated models.

III. NUMERICAL RESULTS: LIMITING CASES

A. $U = V_{ij} = 0$

Although the band limit of zero electron correlation is well understood, discussions of the eigenstates within the exciton basis is nevertheless useful, since it helps us understand the evolution of the delocalized $1B_u$ into a localized exciton when electron correlations are included. Similar evolutions of excited A_g states are also of interest. In particular, we will show later that physically, the $2A_g$ state of the band limit and the mA_g state for the Ohno parameters are very similar, thereby providing an intuitive understanding of the large dipole coupling between the correlated $1B_u$ and the mA_g .¹⁵⁻²³

Our exact numerical results are for $N=5$ and with $\delta = 0.1$. The $1A_g$ ground state is shown in Fig. 5(a), where we have included exciton-basis VB diagrams that make the strongest contributions. As seen in Fig. 5(a), the Hückel ground state has the largest contribution from the Simpson ground state, with additional contributions from diagrams with nearest-neighbor CT. Ground-state stabilization is due primarily to CT between neighboring units.

The optical $1B_u$ state and the $2A_g$ state are shown in Figs. 5(b) and 5(c). Both the $1B_u$ and the $2A_g$, $1e-1h$ excitations in the MO representation, are seen to be primarily one excitations with additional weaker contributions from two excitations in the exciton basis. The two-excitation contribution to the $1B_u$ and the $2A_g$ is a direct consequence of the one-excitation CT contribution to the $1A_g$ [see Fig. 5(a)]. In spite of the significant contributions by diagrams that are two excitations with respect to the Simpson ground state, we will show below that the eigenstates are true one excitations with respect to the *true* $1A_g$ eigenstate.

The delocalized band nature of the $1B_u$ is clear from the wave function shown in Fig. 5 (b). Note, for example, that all one excitations contribute nearly equally to the wave function, with the exception of the diagram with nearest-neighbor CT near the center of the chain (with coefficient 0.39) and the two diagrams in which the both the electron and the hole are at the chain ends (each with coefficients -0.12). The

$$\begin{aligned}
(a) \ 1A_g : & \quad +0.69 \begin{array}{c} \overline{\text{---}} \\ \text{---} \end{array} - 0.41 \begin{array}{c} \overline{\text{---}} \\ \text{---} \end{array} - 0.40 \begin{array}{c} \overline{\text{---}} \\ \text{---} \end{array} + 0.16 \begin{array}{c} \overline{\text{---}} \\ \text{---} \end{array} + 0.14 \begin{array}{c} \overline{\text{---}} \\ \text{---} \end{array} + 0.12 \begin{array}{c} \overline{\text{---}} \\ \text{---} \end{array} + 0.12 \begin{array}{c} \overline{\text{---}} \\ \text{---} \end{array} \\
(b) \ 1B_u : & \quad +0.39 \begin{array}{c} \overline{\text{---}} \\ \text{---} \end{array} - 0.27 \begin{array}{c} \overline{\text{---}} \\ \text{---} \end{array} - 0.25 \begin{array}{c} \overline{\text{---}} \\ \text{---} \end{array} - 0.25 \begin{array}{c} \overline{\text{---}} \\ \text{---} \end{array} + 0.25 \begin{array}{c} \overline{\text{---}} \\ \text{---} \end{array} + 0.25 \begin{array}{c} \overline{\text{---}} \\ \text{---} \end{array} - 0.24 \begin{array}{c} \overline{\text{---}} \\ \text{---} \end{array} \\
& \quad -0.21 \begin{array}{c} \overline{\text{---}} \\ \text{---} \end{array} + 0.16 \begin{array}{c} \overline{\text{---}} \\ \text{---} \end{array} + 0.16 \begin{array}{c} \overline{\text{---}} \\ \text{---} \end{array} + 0.15 \begin{array}{c} \overline{\text{---}} \\ \text{---} \end{array} - 0.15 \begin{array}{c} \overline{\text{---}} \\ \text{---} \end{array} - 0.13 \begin{array}{c} \overline{\text{---}} \\ \text{---} \end{array} - 0.12 \begin{array}{c} \overline{\text{---}} \\ \text{---} \end{array} \\
& \quad -0.12 \begin{array}{c} \overline{\text{---}} \\ \text{---} \end{array} \\
(c) \ 2A_g : & \quad +0.41 \begin{array}{c} \overline{\text{---}} \\ \text{---} \end{array} + 0.37 \begin{array}{c} \overline{\text{---}} \\ \text{---} \end{array} - 0.28 \begin{array}{c} \overline{\text{---}} \\ \text{---} \end{array} - 0.26 \begin{array}{c} \overline{\text{---}} \\ \text{---} \end{array} - 0.23 \begin{array}{c} \overline{\text{---}} \\ \text{---} \end{array} + 0.20 \begin{array}{c} \overline{\text{---}} \\ \text{---} \end{array} - 0.19 \begin{array}{c} \overline{\text{---}} \\ \text{---} \end{array} \\
& \quad + \left[0.15 \begin{array}{c} \overline{\text{---}} \\ \text{---} \end{array} + 0.15 \begin{array}{c} \overline{\text{---}} \\ \text{---} \end{array} \right] \\
(d) \ 3A_g : & \quad +0.20 \begin{array}{c} \overline{\text{---}} \\ \text{---} \end{array} + 0.17 \begin{array}{c} \overline{\text{---}} \\ \text{---} \end{array} - 0.16 \begin{array}{c} \overline{\text{---}} \\ \text{---} \end{array} - 0.16 \begin{array}{c} \overline{\text{---}} \\ \text{---} \end{array} + 0.15 \begin{array}{c} \overline{\text{---}} \\ \text{---} \end{array} + 0.15 \begin{array}{c} \overline{\text{---}} \\ \text{---} \end{array} - 0.14 \begin{array}{c} \overline{\text{---}} \\ \text{---} \end{array} \\
& \quad -0.14 \begin{array}{c} \overline{\text{---}} \\ \text{---} \end{array} - 0.14 \begin{array}{c} \overline{\text{---}} \\ \text{---} \end{array}
\end{aligned}$$

FIG. 5. Dominant contributions to the important Hückel wave functions within the exciton basis. Here, and in all subsequent figures, only one diagram corresponding to the full set related by mirror-plane and charge-conjugation symmetries are shown. The $1B_u$ and $2A_g$ are one excitation relative to the exact $1A_g$, in spite of considerable two-excitation contributions (relative to the Simpson ground state) to these wave functions (see text). The $2A_g$ is seen to be related to the $1B_u$ by charge transfer between MO's with the same λ . The two-excitation $3A_g$ is seen to be uncorrelated.

large contribution by the chain-center CT diagram and the small contributions by the two diagrams with electron and hole at chain ends are both consequences of the finite size effects associated with an open short chain. The chain-center CT diagram is coupled to the largest number of diagrams through one application of H_{CT}^{inter} , and is therefore the most ‘‘favorable’’ diagram in a finite chain. Similarly, the diagrams with a singlet bond terminating on the ends of the chain are coupled to the least number of other CT diagrams by H_{CT}^{inter} , and are least favorable. In the long chain limit, this distinction between CT diagrams vanishes, and all Frenkel and CT diagrams will contribute equally to the $1B_u$ wave function.

The Hückel $2A_g$ can be simply characterized as a CT eigenstate with respect to the $1B_u$ eigenstate. There is almost a one-to-one correspondence between the exciton basis diagrams of the $2A_g$ and the $1B_u$: each diagram of the former can be obtained by one application of the bonding-to-bonding or antibonding-to-antibonding terms in H_{CT}^{inter} on a suitable diagram of the $1B_u$. Among all A_g states, the $2A_g$ has the largest dipole coupling with the $1B_u$ in the Hückel limit.²⁰ This large dipole coupling of the $2A_g$ is a direct consequence of its CT character with respect to the $1B_u$. As discussed above, the nature of the current operator [see Eqs. (17) and (18) and the discussion following them] dictates that the dipole coupling is largest between eigenstates that consist of many-electron configurations related by CT between MO's with the *same* λ . Since the Hückel $1B_u$ and $2A_g$ are related precisely by such CT, the large dipole coupling between them is easy to understand.

In the MO basis, both the Hückel $1B_u$ and $2A_g$ are $1e-1h$ excitations with respect to the $1A_g$. In the exciton basis, however, the number of excitations is no longer a good quantum number. In spite of this, it is still possible to gain quali-

tative understanding of the nature of excited states from exact calculations of the number of excitations η_s for each state s , where

$$\eta_s = \left\langle \sum_{i,\sigma} a_{i,2,\sigma}^\dagger a_{i,2,\sigma} \right\rangle_s - \left\langle \sum_{i,\sigma} a_{i,2,\sigma}^\dagger a_{i,2,\sigma} \right\rangle_{1A_g}. \quad (19)$$

η_s measures the true number of excitations, relative to the exact $1A_g$, for state s . Our calculated η_{1B_u} and η_{2A_g} are 0.865 and 0.804, respectively. The numbers are understandably not exactly 1.0, but are nevertheless close to this. We point out two important features. First, the one-excitation character of the $1B_u$ and the $2A_g$ could have been anticipated from the natures of the dominant exciton basis VB diagrams for these eigenstates (Fig. 5). Second, within the exciton basis, η_{2A_g} is slightly smaller than η_{1B_u} , although both are $1e-1h$ states within the MO basis. We will see later that in the correlated case, the $1B_u$ and the A_g state to which it is most strongly coupled both have η_s values that are close to 1.

For the subset of eigenstates that are predominantly one excitation with respect to the exact $1A_g$ (η_s close to 1), we define another physical quantity that is used to distinguish between individual members of the subset. This is the average bond length b_s of the CT bonds in the one-excitation contributions to the state s ,

$$b_s = \sum_i c_i^2 l_i / \sum_i c_i^2, \quad (20)$$

where l_i is the length (in units) of the bond in a given one-excitation diagram and c_i is the coefficient of that diagram in the eigenfunction. Weak contributions by diagrams with two and higher excitations are therefore ignored in the above definition. This is reasonable, since, as mentioned above,

TABLE I. Normalized dipole couplings (electronic charge = 1, lattice constant = 1) between A_g states and the $1B_u$ ($k=0$ exciton) and $2B_u$ (lowest $k \neq 0$ exciton) for $N=5$, for $t_2=0$. All excited A_g states below the $18A_g$, the lowest biexciton, have zero dipole coupling with the one-exciton states $1B_u$ and the $2B_u$. The $19A_g$ is the lowest nonzero k biexciton. Two-exciton continuum states (see text) above the threshold state, the $36A_g$, are not shown. In the long-chain limit, A_g states that have large nonzero dipole couplings with the $1B_u$ will have zero dipole coupling with the $2B_u$ and vice versa.

| A_g state | $\langle kA_g \hat{\mu} 1B_u \rangle$ | $\langle kA_g \hat{\mu} 2B_u \rangle$ |
|-------------|---|---|
| 1 | 1.0 | 0.561 |
| 2 | 0.0 | 0.0 |
| 18 | 0.806 | 0.151 |
| 19 | 0.195 | 0.713 |
| 36 | 0.903 | 0.527 |

(i) intraunit ‘‘vertical’’ excitation, and (ii) interunit CT. Unlike the Hückel case, only the first term contributes in the $t_2=0$ limit. We therefore expect a strong dipole coupling between the $1A_g$ and the $1B_u$, as these states differ by single vertical excitations. Further dipole excitation from the $1B_u$ can only lead to a pair of singlet excitations, and thus we expect (and find) that the states previously identified as SS by their wave functions (i.e., the $18A_g$ and $36A_g$) are both strongly dipole coupled to the $1B_u$. One important result is that the dipole coupling between the $2A_g$ and the $1B_u$ is identically zero in the limit $t_2=0$. This is easily understood. From the expression for the current operator, direct dipole excitation of the $1B_u$ generates only the two excitations that are analogs of the diagrams (d) and (g) of Fig. 1. Then, $\langle 1B_u | \hat{\mu} | TT \rangle = \langle g | TT \rangle = \langle g | 2f + g \rangle = 0$, since $\langle g | g \rangle = 1$ and $\langle f | g \rangle = -1/2$. Thus, the TT diagrams play no role in optical processes in the limit $t_2=0$. We will show below that with $t_2 \neq 0$, both the $1B_u$ and the $2A_g$ mix with CT configurations and their dipole coupling no longer vanishes. However, it is clear that any dipole coupling between the $2A_g$ and the $1B_u$ has to originate almost entirely from the CT components of the $2A_g$, and the two-excitation components make no contribution. This has been pointed out previously within configuration interaction calculations using the MO basis,²⁰ as well as in other recent exciton-basis calculations in the regime of large bond alternation,⁴⁶ but the present results are particularly transparent.

Within the $t_2=0$ limit the effects of Coulomb interactions are clear. The single excitations are split into Frenkel excitons and higher energy CT diagrams. Similarly, the most relevant doubly excited states are split into the much discussed low-energy TT states^{52,53} and higher energy SS states. The SS states themselves are split into bound biexciton and free two-exciton states. In addition to these, there exist two excitations with separated or uncorrelated electron and hole pairs. These states can never be reached in nonlinear optical absorption experiments, and are thus irrelevant to our discussions here. For the same reason three and four excitations have been not discussed, although all these eigenstates are obtained in our calculations. We can summarize the energetic ordering of the relevant states as

$$TT < F < CT < TTT < BX < 2X, \quad (21)$$

where F are Frenkel exciton states, and BX and $2X$ are biexciton and two-exciton continuum states, respectively.

IV. NUMERICAL RESULTS: COMPLETE HAMILTONIAN

We now discuss numerical results for $N=5$ with the full PPP–Ohno Hamiltonian with $t_2 \neq 0$. We choose two different parameter sets, (a) $\delta=0.07$, corresponding to transpolyacetylene and (b) $\delta=0.3$, believed to describe the polysilanes within the Sandorfy-C model (we ignore the fact that U/t in silicon-based systems may be somewhat smaller than that in carbon based systems; our purpose here is to compare the effects of large and small bond alternation only).^{22,23} The addition of nonzero t_2 causes admixing between the basic exciton-basis VB diagrams that characterize the $t_2=0$ wave functions, and the analysis of wave functions necessarily become more complicated. From Eq. (21), there are two possible consequences of such admixing. First, the admixing is weak (i.e., all wave functions can still be classified as *predominantly* TT , CT , etc.) and the principal consequence of nonzero t_2 is a reordering of energy states, especially at the boundaries between any two neighboring classes of states. The second possibility is that the admixing between different classes of states is strong, and classification of the eigenstates becomes more involved.

A. $\delta=0.07$

For weak bond alternation, we will see that in all cases the admixing is weak, and energy reordering is the principal result of the addition of nonzero t_2 . Dominant contributions to the optically relevant wave functions for this case are shown in Figs. 7 and 9. Relevant energies, normalized transition dipole moments, and other wave-function characteristics are summarized in Table II.

$1A_g$: The $1A_g$, shown in Fig. 7(a), is still dominated by the Simpson ground state, with now nonzero contributions from both nearest-neighbor CT diagrams (as in the Hückel ground state) as well as doubly excited units (as in the $t_2=0$ ground state).

$1B_u$: The $1B_u$ [see Fig. 7(b)] is now an admixture of Frenkel excitons and CT diagrams. In contrast to the Hückel $1B_u$, however, the contributions by CT diagrams decrease rapidly as the length of the CT bond increases. This decrease is strong enough that the contribution by the diagram with a CT bond between third neighbors is less than half that of the CT diagram with a bond between nearest neighbors (note that these have the same weight in the Hückel $1B_u$), and the diagram with the longest CT bond makes no perceptible contribution to the wave function. This is a strong signature of the localized exciton character of the $1B_u$.⁴² One interesting feature of the $1B_u$ exciton is that the contribution by the Frenkel exciton diagram is smaller than that by diagrams with nearest-neighbor CT, a feature that had been observed earlier within an exact solution to the exciton problem in the $U \rightarrow \infty$ limit.³³ The calculated average bond length for the Frenkel and CT contributions to the $1B_u$ exciton is $b_{1B_u} = 0.98$, halfway between the $t_2=0$ bond length of 0.5, and the Hückel length of 1.44. The relatively large b_{1B_u} implies that all two-exciton states are at relatively high energy com-

$14A_g$ is clearly related to the $18A_g$ with $t_2=0$, with three minor differences, all consequences of nonzero t_2 . First, the $14A_g$ shown here is the lowest $k \neq 0$ biexciton. The $k=0$ biexciton within the complete Hamiltonian, though discernible as such, is at slightly lower energy and is strongly mixed with the highest energy TTT diagrams. A second difference between the $14A_g$ here and the $18A_g$ with $t_2=0$ is the addition of interunit charge transfer, leading to contributions by localized two excitations in which one of the two excited electrons or holes has migrated to a neighboring unit [see Figs. 1(e) and 9]. Finally, the $14A_g$ in Fig. 9 has contributions from one-excitation CT diagrams. The $19A_g$ and $25A_g$ here are both similar to the $36A_g$ with $t_2=0$, in that these wave functions are dominated by contributions that are two independent excitons. Once again, weak one-excitation CT contributions are seen. The widths of the individual excitons in these two-exciton states are considerably smaller than the width of the $1B_u$ exciton in Fig. 7(b), which is a finite size effect that is understandable: the $N=5$ chain simply does not have enough physical space to accommodate two optimal excitons. Since the energy of the $1B_u$ exciton is lowered considerably by the electron-hole delocalization contributing to its width, the small widths of the individual excitons in the finite chain two-exciton states imply that the energies of all two-exciton states in short chains would be considerably above $2 \times E(1B_u)$.²⁰ Thus, even as our short-chain calculations are exact, no signature of exciton-exciton binding can be obtained from the energetic consideration which is valid in the long-chain limit, viz., two-exciton states below $2 \times E(1B_u)$ are bound. Precisely because of this, an alternate criterion based on transition dipole couplings (see below) was developed in Ref. 20. The advantage of the present exciton-basis calculation over our previous work lies in that from the pictorial descriptions of the two-exciton states, the bound biexciton nature of the $14A_g$ and the free two-exciton character of the $19A_g$ and the $25A_g$ are obvious. The absence of delocalized two-exciton diagrams in the $14A_g$ on the one hand, and the absence of the localized two excitations in the $19A_g$ and the $25A_g$ on the other, indicates that CI does not lead to the appreciable mixing of localized and delocalized two-exciton diagrams. This, in turn, is a distinct signature of the bound biexciton character of the $14A_g$.

B. $\delta=0.3$

Increasing δ leads to competition between two different correlation effects. On the one hand, U/t_1 decreases, and the energies of the TT diagrams increase relative to the Frenkel and CT diagrams, pushing the $2A_g$ above the $1B_u$. At the same time, however, larger U/t_2 leads to increased exciton binding, as interunit charge transfer becomes less energetically favorable. Within the exciton basis, the higher energy of the lowest A_g states causes strong mixing between the basic TT and CT diagrams, leading to eigenstates that are linear combinations of the type $(CT + TT)$, $(CT + TTT)$, etc. We focus below on the A_g states that are most strongly dipole coupled to the $1B_u$, as these are the states that are most relevant for nonlinear optical processes. We do not show the $1B_u$ explicitly, as it largely resembles the $1B_u$ state for $\delta=0.07$. The major difference is that b_{1B_u} here is 0.91, as compared to 0.98 in the previous case, implying a greater

TABLE III. The energies (in units of $|t|=2.4$ eV) and wave-function characteristics of the lowest seven excited states $\delta=0.3$. The transition dipole couplings with the $1B_u$ are relative to $\langle 1A_g | \hat{\mu} | 1B_u \rangle$.

| A_g State | Energy | $\langle kA_g \hat{\mu} 1B_u \rangle$ | η_s | b_s |
|-------------|--------|---|----------|-------|
| 1 | 0 | 1.0 | 0 | 1.0 |
| 2 | 2.66 | 0.81 | 1.49 | 1.52 |
| 3 | 2.99 | 0.14 | 1.48 | 1.06 |
| 4 | 3.31 | 0.40 | 1.83 | 1.14 |
| 5 | 3.60 | 0.14 | 1.81 | 1.30 |
| 6 | 3.69 | 0.97 | 1.69 | 1.71 |
| 7 | 3.79 | 0.98 | 1.56 | 2.61 |

Frenkel contribution to the $1B_u$ wave function, and therefore an increase in exciton binding energy with increasing δ .

The energies, transition dipole couplings with the $1B_u$, η_s and b_s for the states $2A_g - 7A_g$ are shown in Table III. The $2A_g$, $6A_g$, and $7A_g$ are now all strongly dipole coupled to the $1B_u$. This is due to the large CT component in all the wave functions, as shown in Fig. 10, where we show the $2A_g$ and $7A_g$ for $\delta=0.3$. These states are both (as are all of $2A_g - 12A_g$) strong mixtures of TT , $TT \otimes CT$, and CT diagrams (note the nearly 2:1 contributions by the diagrams within the parentheses in Fig. 10). We characterize the three states $2A_g$, the $6A_g$, and the $7A_g$ as predominantly $TT + CT$, which agrees with the η_s values of nearly 1.5, intermediate between that for purely TT (2.0) and purely CT (1.0). Unlike the small δ case, therefore, classification into predominantly TT or predominantly CT is no longer possible. If one defines the mA_g now as the state that makes the strongest contribution to third-order optical nonlinearity, identification of this state from dipole couplings, or from Fig. 10, is thus no longer possible. However, it has previously been shown that a large dipole coupling to the $1B_u$ does not necessarily imply a strong contribution to third-order nonlinear optical processes, because of cancellations arising from nonlinear pathways that involve the same B_u state and different B_u states.²⁰ We can then use the calculated two-photon absorption to identify the mA_g , defined as above.

In Fig. 11 we show the calculated two-photon absorption (TPA) for $N=5$ with $\delta=0.3$. As expected, the contribution from the $2A_g$ (at $2\hbar\omega/E(1B_u) \approx 1.05$) is negligible, *in spite of its large dipole coupling to the $1B_u$* (see Table III). This simply requires that the energies of the two B_u states to which the $2A_g$ is coupled are close to each other.²⁰ The strong TPA in Fig. 11 is to the $6A_g$ and the $7A_g$. The TPA calculations were also performed by ignoring one of these two states but retaining the other (i.e., these modified calculations were done twice). In this fashion, it was determined that the two states $6A_g$ and $7A_g$ contribute nearly equally to the strong TPA, and therefore both of these exhibit mA_g behavior.

The above results then raise the following important issue. In the small δ case ($2A_g$ below the $1B_u$), the charge-transfer character of the mA_g is obvious from the η_s values of this state and neighboring states. For large δ , the η_s for the $2A_g$, the $6A_g$, and the $7A_g$ are nearly the same. Thus whether or not the mA_g states(s) can be considered as the

$$\begin{aligned}
2A_g : & \quad + \left[0.48 \text{---} \text{---} \text{---} \text{---} + 0.26 \text{---} \text{---} \text{---} \text{---} \right] - 0.36 \text{---} \text{---} \text{---} \text{---} - \left[0.28 \text{---} \text{---} \text{---} \text{---} + 0.19 \text{---} \text{---} \text{---} \text{---} \right] - 0.24 \text{---} \text{---} \text{---} \text{---} \\
& \quad + 0.23 \text{---} \text{---} \text{---} \text{---} - \left[0.21 \text{---} \text{---} \text{---} \text{---} + 0.13 \text{---} \text{---} \text{---} \text{---} \right] + 0.20 \text{---} \text{---} \text{---} \text{---} + \left[0.20 \text{---} \text{---} \text{---} \text{---} + 0.11 \text{---} \text{---} \text{---} \text{---} \right] \\
7A_g : & \quad + \left[0.49 \text{---} \text{---} \text{---} \text{---} + 0.19 \text{---} \text{---} \text{---} \text{---} \right] + \left[0.42 \text{---} \text{---} \text{---} \text{---} + 0.21 \text{---} \text{---} \text{---} \text{---} \right] + 0.33 \text{---} \text{---} \text{---} \text{---} - 0.26 \text{---} \text{---} \text{---} \text{---} \\
& \quad + \left[0.23 \text{---} \text{---} \text{---} \text{---} + 0.09 \text{---} \text{---} \text{---} \text{---} \right] - 0.23 \text{---} \text{---} \text{---} \text{---} - \left[0.22 \text{---} \text{---} \text{---} \text{---} + 0.13 \text{---} \text{---} \text{---} \text{---} \right] \\
14A_g : & \quad + 0.48 \text{---} \text{---} \text{---} \text{---} - 0.38 \text{---} \text{---} \text{---} \text{---} + 0.36 \text{---} \text{---} \text{---} \text{---} + 0.22 \text{---} \text{---} \text{---} \text{---} + \left[0.18 \text{---} \text{---} \text{---} \text{---} + 0.13 \text{---} \text{---} \text{---} \text{---} \right] - 0.18 \text{---} \text{---} \text{---} \text{---} \\
& \quad + 0.15 \text{---} \text{---} \text{---} \text{---}
\end{aligned}$$

FIG. 10. Dominant contributions to the wave functions of the $2A_g$, the $7A_g$ (mA_g), and the $14A_g$ (lowest biexciton) for $\delta=0.3$. Both the $2A_g$ and the $7A_g$ are now $TT+CT$, but the bond length b_{7A_g} is considerably larger than b_{2A_g} and b_{1B_u} (see text). Note the nearly 1:1 contribution by the diagrams within the parentheses in the $14A_g$.

lower threshold of the continuum band for large δ cannot be determined from η_s calculations. The very strong CT components in the states being considered, however, allow us to compare their bond lengths b_s , which are also included in Table III. The very large b_{7A_g} , compared to the b_{1B_u} of (0.91), indicates the charge-transfer character of the $7A_g$. As in the case of small δ , therefore, strong contribution to third-order optical nonlinearity are by a charge-transfer A_g state and any A_g state that is proximate to this state. In contrast to the $7A_g$, the particle-hole separation in the $2A_g$ is small, and it contributes weakly to third-order processes. The charge-transfer character of the mA_g , and the more localized behavior of the lower A_g states, ensures that the A_g state that makes the strongest contribution to third-order optical nonlinearity also gives a lower limit for the exciton binding energy in conjugated polymers.

In Fig. 10 we also show the wave function of the $14A_g$, which is the lowest biexciton state for $\delta=0.3$. In addition to

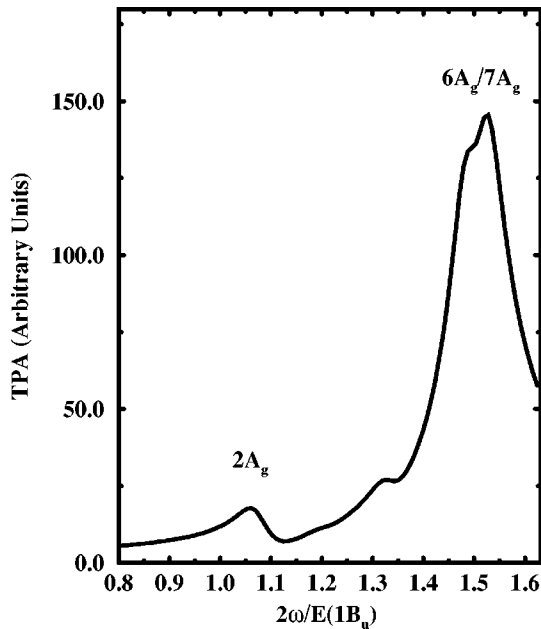


FIG. 11. Calculated TPA for $\delta=0.3$.

the doubly excited single unit, which characterizes the biexciton at $\delta=0.07$ (see Fig. 9), we find nonzero contribution from the ‘‘crossed’’ diagrams of Fig. 3(a). This is in contrast to the work of Ishida,⁴⁴ in which the biexciton consists solely of diagrams of the type (g) in Fig. 1. The origin of the discrepancy is as follows. Figure 1(g) corresponds to the linear combination of the configuration-space configurations 2002, 2020, 0202, and 0220, where 0(2) indicates an empty (doubly occupied) atom. Thus Fig. 1(g) obviously contributes strongly to the biexciton wave functions. However, the repulsive interaction due to neighboring atoms with the same charges is also extreme within this diagram. The binding that occurs within the approximate calculations then has to be an artifact of the neglect of important terms within the full PPP Hamiltonian (see Sec. II C). In contrast, the ‘‘crossed’’ diagram in Fig. 3, can be viewed as the combination $-(2|f\rangle + |g\rangle) - |g\rangle$. This diagram has strong TT contributions, and it is the configuration interaction with lower energy TT configurations that stabilizes the true BX wave function relative to diagram (g) alone.

The charge-transfer character of the mA_g , and the demonstration that the true biexciton occurs at even higher energy, raises an interesting possibility in the context of third-order optical nonlinearity in poly(di-n-hexyl-polysilane) (PDHS).²³ The two-photon absorption (TPA) spectrum of this material is characterized by a narrow, strong absorption at $2\hbar\omega = 1.2E_g$ (where E_g is the optical gap), with a weaker broad feature starting at around $2\hbar\omega = 1.5E_g$.²³ These have previously been assigned to the $2A_g$ and the mA_g ,²³ where the authors characterized the mA_g as the biexciton. Additionally, in order to fit the experimental spectrum these authors introduced ad hoc linewidth parameters that were rather artificial. Specifically, the linewidth of the $2A_g$ was taken to be smaller than the linewidths of all other states by a factor of 75. This gave a sharp TPA to the $2A_g$, with a second intense TPA to the remaining A_g states, with overall relative intensity of the higher energy TPA considerably larger than that observed in the experiment. Our calculated TPA in Fig. 11 and the discussion above presents an alternate interpretation that does not require this extreme narrow linewidth for the $2A_g$. Since TPA to the $2A_g$ is rather weak, the low-energy

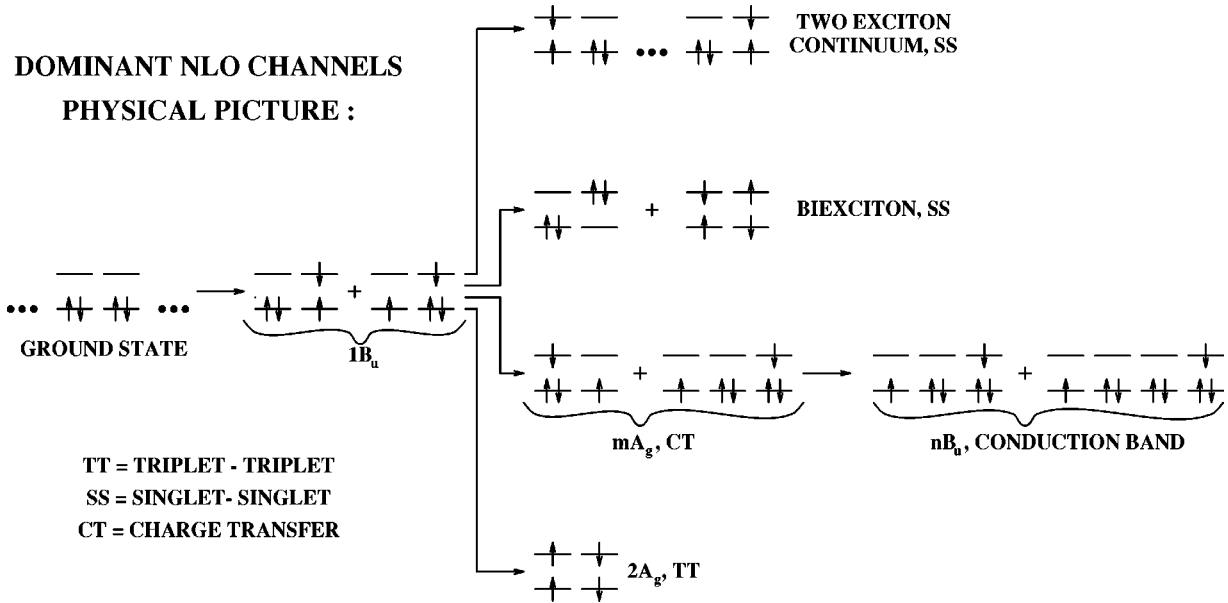


FIG. 12. Schematic of nonlinear optical processes in the exciton basis. Configurations, rather than VB diagrams are shown, as the consequence of the application of the current operator is clearer. Each configuration can be obtained by one application of the current operator to either of the two configurations to which it is linked by an arrow. The actual dipole coupling between the $1A_g$ and nB_u eigenstates is weak but nonzero (see text).

TPA can simply be assigned to the mA_g . The CT character of this state, even for $\delta=0.3$, explains its occurrence below the threshold of the continuum band.⁵⁵ The cancellation effect in the nonlinear optical channels that reduces the TPA to A_g states in the vicinity of the mA_g (see Fig. 11) increases with chain length,²⁰ and can therefore naturally explain the narrow linewidth of the low-energy TPA in PDHS.²³ High-energy TPA is then assigned to the true biexciton states (see Fig. 10) within our picture [the biexciton states in our calculation are above $2 \times E(1B_u)$ because of finite size effects, and are thus not shown in Fig. 11].

To summarize this subsection, increasing δ induces large mixing between the TT and CT diagrams, and excited states that are linear combinations of these occur above the $1B_u$. The very lowest of these A_g states have CT bonds that are short, and the mA_g , which occurs at slightly higher energy, is still the lowest A_g state that is of charge-transfer character relative to the $1B_u$. The true biexcitons are at even higher energy.

V. NONLINEAR OPTICAL CHANNELS

As has been emphasized by different groups, individual third-order nonlinear optical channels for centrosymmetric linear π -conjugated systems can be written as

$$1A_g \rightarrow jB_u \rightarrow kA_g \rightarrow lB_u \rightarrow 1A_g,$$

where each arrow denotes a dipole-allowed process. In the event of exciton formation, significant contribution to the overall nonlinearity requires that at least one of j and l (but not necessarily both) is 1. Based on the natures of the wave functions and the dipole couplings between them, we are able to describe the dominant nonlinear optical channels qualitatively within the exciton basis. The case of small δ is shown schematically in Fig. 12 where we have described each eigenstate by the most representative exciton-basis con-

figurations (rather than the $S=0$ VB diagrams, since vertical and interunit excitations are easier to visualize within the $S_z=0$ representation), and where we have chosen $j=1$. Each arrow in Fig. 12 represents both a forward (excitation) and a reverse (deexcitation) process, and denotes the result of the application of the current operator [Eq. (17)] on either of the configurations connected by the arrow.

In Fig. 12, optical absorption from the ground state leads to the $1B_u$ exciton, which has both Frenkel and CT contributions. The creation of a second excitation on the same or a neighboring unit can lead to either the $2A_g$ or the biexciton, while the creation of a second exciton far from the first gives the threshold of the two-exciton continuum. All of these processes involve either the first term in the expression for the current operator in Eq. (17) or the second term with $\lambda \neq \lambda'$. In addition to the above processes, CT to neighboring units, corresponding to $\lambda = \lambda'$ in the second term of Eq. (17), gives the mA_g . The large dipole coupling between this state and the $1B_u$ (for realistic δ) is simply a consequence of Eq. (18). We have shown in the previous sections that the wave function of the interacting mA_g is nearly identical to that of the Hückel $2A_g$. The difference in the particle-hole separation between the correlated mA_g and the $1B_u$ is also similar to the same quantity between the uncorrelated $2A_g$ and the $1B_u$. Excitation from the mA_g leads to further electron-hole separation, leading to the nB_u state, which has previously been identified as the threshold state of the electron-hole continuum.¹⁹ Although Fig. 12 formally suggests a vanishing dipole coupling between the $1A_g$ and the nB_u , this is merely a consequence of ignoring the small but nonzero contributions by diagrams with neighboring CT in the nB_u (or more distant CT in the $1B_u$) in the figure. In reality, $\langle 1A_g | \hat{\mu} | nB_u \rangle$ is nonzero, and leads to a weak nonlinear optical channel $1A_g \rightarrow 1B_u \rightarrow mA_g \rightarrow nB_u \rightarrow 1A_g$, in addition to the strong processes depicted in Fig. 12.^{15,16,19,20}

We do not give a separate figure for the case of larger δ . Our discussions in Sec. IV make it clear that the only difference in this case is that there exist only three distinct classes of two-photon states, as opposed to four for small δ . The TT and CT states are not distinct here, and both the $2A_g$ and the mA_g are $TT+CT$.

Inspection of Fig. 12 and our eigenstates in Sec. IV explains the qualitative similarity between the proposed mechanisms for nonresonant nonlinear optical nonlinearity within the singles-CI calculations^{15–17,43} and within the short-chain FCI calculations, as interpreted by us.^{18–21,36} Essentially, the strongest effects of CI are to cause the energy splittings between the Frenkel and CT one excitations on the one hand, and TT and SS two-excitations on the other. Since TT states do not have dipole coupling with the $1B_u$, the characterization of eigenstates as predominantly one and two excitations is approximately true. Consequently, in the low-frequency region where the contribution by high-energy SS states are weak, one excitations determine the nonresonant optical nonlinearity.

VI. THE EVOLUTION OF WAVE FUNCTIONS

The above sections clearly indicate that while there exist only simple $1e-1h$ and $2e-2h$ A_g states at in the Hückel limit, for moderate Coulomb interactions there occur four distinct classes of optically relevant two-photon states at small δ . Although our interest lies in understanding the linear and nonlinear optical properties of conjugated polymers, it is of theoretical interest to address the question of how the strong Coulomb interaction regime is reached from moderate interactions. The strong Coulomb interaction regime has been discussed within the $U \rightarrow \infty$ limit before.²⁰ The relevant quantity for the characterization of wave functions is no longer the number of excitations η_s across excitonic units, as it is for moderate interactions, but rather N_2 , the number of carbon atoms that are occupied by two electrons. The $1A_g$ in the $U \rightarrow \infty$ limit is dominated by the configuration $\dots 111111 \dots$, where the numbers denote site occupancies by electrons. The $1B_u$, for large nearest-neighbor intersite Coulomb interactions is the linear combination $(\dots 112011 \dots) - (\dots 110211 \dots)$, while the mA_g is a linear combination of $(\dots 112011 \dots) + (\dots 110211 \dots)$ and $(\dots 1121011 \dots + \dots 1101211 \dots)$, with relative weights of the nearest-neighbor excitonic and the charge-transfer contributions determined by the actual details of the theoretical model being considered. Similarly, the nB_u is now an appropriate combination of $(\dots 1121011 \dots) - (\dots 1101211 \dots)$ and $(\dots 11211011 \dots) - (\dots 11011211 \dots)$. The $2A_g$ is a spin-wave state, and the biexciton and the two-exciton continuum states are now the $\dots 11202011 \dots$ configuration, and the configurations $\dots 112011 \dots 12011 \dots$, respectively. These are the only kinds of two-photon states that are arrived at by two applications of the current operator on the ground-state configuration. One then sees that the fundamental description of nonlinear optical channels is the same at both moderate and strong Coulomb interactions.

The only difference between moderate and strong Coulomb interactions lies in the actual compositions of the wave functions. This is best illustrated by the examination

of the mA_g and the biexciton wave functions. As discussed in the above, the configuration-space wave function $(\dots 11120111 \dots) + (\dots 11102111 \dots)$ makes a strong contribution to the strongly correlated mA_g . However, precisely this same configuration describes the exciton-basis diagram with a doubly excited unit that constitutes the biexciton in the moderate Coulomb interaction case (see the $14A_g$ in Fig. 10). The configurations that describe the mA_g and the biexciton then change continuously as the Coulomb correlation parameters are increased from moderate values, so much so that for strong correlations the doubly excited dimer is a component of the mA_g and not the biexciton. Of course, all other wave functions change accordingly, since the relationship between them continues to be as suggested in Fig. 12, but only between the mA_g and the biexciton is there a continuous reshuffling of the same configuration.

VII. CONCLUSIONS

In conclusion, we have presented in detail a discussion of the energy spectrum and dominant nonlinear optical channels for linear polyenes within a diagrammatic exciton-basis VB theory. The present exciton theory includes all interactions within the PPP Hamiltonian. The chief advantage of this technique is that physical, pictorial descriptions of exact eigenstates are obtained, thereby making the relationships between the excited states clear, and allowing us to extend the central concepts to the long-chain polymeric limit. Our most important result is that the relationship between the correlated mA_g and the $1B_u$ exciton is the same as between the Hückel $2A_g$ and the $1B_u$: in both cases the A_g state in question is obtained from the respective $1B_u$ by charge transfer between MO's of neighboring units that are either both bonding or both antibonding. The large dipole coupling between the $1B_u$ and the mA_g is a simple consequence of the nature of the current operator: charge transfers between a bonding (antibonding) and an antibonding (bonding) MO, though allowed, is less favored. Eigenstates that belong to classes other than CT are obtained from the $1B_u$ by precisely such less favored charge-transfer processes. Our earliest work on this subject¹⁸ focused on short-range interactions only, and had claimed that the mA_g is necessarily pinned between the $1B_u$ and the $2B_u$. With long-range interactions, this is not true, as the exciton band acquires greater width in this case. Nevertheless, as discussed in Sec. IV, the lowest charge-transfer B_u state occurs above the mA_g . Even when the $2A_g$ occurs above the $1B_u$, the A_g state that makes the largest contribution to the third-order optical nonlinearity is of charge-transfer character and is higher than the $2A_g$. Although the $2A_g$ in this case is no longer purely TT , the particle-hole separation is small in this state. This has a very important consequence as far as the current discussions of excitonic effects in π -conjugated polymers are concerned, viz., the experimental determination of the mA_g must necessarily give a lower limit for the excitonic binding energy. Whether the mA_g is closer to the $1B_u$ or to the band threshold has also been a topic of discussion. In our opinion, this depends on the character of the $1B_u$ exciton itself. If the Frenkel contribution to the $1B_u$ exciton is larger than the nearest-neighbor CT contribution, due to large effective

bond alternation, then the first step in the charge-transfer process costs the most energy, and the mA_g is expected to be close to the band threshold. In systems where the reverse is true (as in the polyenes) the mA_g should be closer to the $1B_u$.

In addition to obtaining a physical description of the low-energy TT and CT states, the VB exciton theory also lends support to the previous ideas of stable biexcitons in π -conjugated polymers. The physical natures of the biexciton are slightly different for small and large bond alternation. Furthermore, the physical nature changes continuously with increasing strength of the Coulomb interaction, while maintaining the same relationship with the $1B_u$ exciton. Finally, even though stable biexcitons might occur in π -conjugated polymers, this does not necessarily imply that a high energy photoinduced absorption (PA), seen in the poly(para-phenylenevinyls)¹² is necessarily a transition from the exciton to the biexciton. Although we had made such an assignment earlier,^{12,21} this should strictly be true only in linear chain systems, for which the exciton-basis VB theory presented here clearly shows that there are only two classes of A_g states (viz., CT and bound SS) to which PA can occur. Recent calculations for polyphenylenes within the exciton-basis VB theory has shown that although the low-

energy excitations in these systems are similar to those in linear chains, at higher energies there occur even parity states whose counterparts do not exist in linear chains.⁵⁶ A different, and more plausible, interpretation of high-energy PA seems possible. These results are presented elsewhere.⁵⁷

We recently learned of the work by Shuai et al. on the nonlinear optical response of long linear polyenes.⁵⁸ The authors use the DMRG approach to calculate the nonlinear optical properties of polyenes that are twice the length investigated here, within the nearest-neighbor extended Hubbard Hamiltonian. The results pertaining to the $2A_g$ and the mA_g are similar to our work. In addition, the calculated TPA spectrum (see Fig. 5 of Ref. 58) of octatetraene within the extended Hubbard Hamiltonian is sparse, and weak TPA to a state whose energy is nearly 1.6 times that of the mA_g is found. Whether or not this very high-energy two-photon state is a biexciton state is clearly of interest.

ACKNOWLEDGMENTS

The authors acknowledge support from the NSF-ECS, the AFOSR, and the ONR through the MURI center (CAMP) at the University of Arizona. We thank the referee for bringing Ref. 58 to our attention.

-
- ¹D. Baeriswyl, D.K. Campbell, and S. Mazumdar, in *Conjugated Conducting Polymers*, edited by H. Kiess (Springer-Verlag, Berlin, 1992).
- ²S. Etemad and Z.G. Soos, in *Spectroscopy of Advanced Materials*, edited by R.J.H. Clark and R.E. Hester (Wiley, New York, 1991).
- ³See, for example, *Proceedings of 2nd International Conference on Optical Probes of Conjugated Polymers and Fullerenes*, edited by Z.V. Vardeny and L.J. Rothberg [Mol. Cryst. Liq. Cryst. A **256** (1994)].
- ⁴See, for example, *Primary Photoexcitations in Conjugated Polymers: Molecular Exciton versus Semiconductor Band Model*, edited by N. Serdar Sariciftci (World Scientific, Singapore, 1997).
- ⁵J.A. Pople, Trans. Faraday Soc. **49**, 1375 (1953); Proc. Phys. Soc. **68**, 81 (1954).
- ⁶R. Pariser and R.G. Parr, J. Chem. Phys. **21**, 466 (1953); **21**, 767 (1953).
- ⁷W.-S. Fann, S. Benson, J.M.J. Madey, S. Etemad, G.L. Baker, and F. Kajzar, Phys. Rev. Lett. **62**, 1492 (1989).
- ⁸B. Lawrence, W.E. Torruellas, M. Cha, M.L. Sundheimer, G.I. Stegeman, J. Meth, S. Etemad, and G.L. Baker, Phys. Rev. Lett. **73**, 597 (1994).
- ⁹G. Weiser and A. Horvath, in *Primary Photoexcitations in Conjugated Polymers: Molecular Exciton versus Semiconductor Band Model*, (Ref. 4), pp. 318–362, and references therein.
- ¹⁰C. Halvorson, T.W. Hagler, D. Moses, Y. Cao, and A.J. Heeger, Chem. Phys. Lett. **200**, 364 (1992); C. Halvorson, R. Wu, D. Moses, F. Wudl, and A.J. Heeger, *ibid.* **212**, 85 (1993).
- ¹¹C. Halvorson and A.J. Heeger, Synth. Met. **71**, 1649 (1995); see also, S. Mazumdar and M. Chandross, in *Primary Photoexcitations in Conjugated Polymers: Molecular Exciton versus Semiconductor Band Model* (Ref. 4), pp. 384–429, for a discussion of this experiment.
- ¹²J.M. Leng, S. Jeglinski, X. Wei, R.E. Benner, Z.V. Vardeny, F. Guo, and S. Mazumdar, Phys. Rev. Lett. **72**, 156 (1994).
- ¹³S.V. Frolov, M. Liess, P.A. Lane, W. Gellermann, Z.V. Vardeny, M. Ozaki, and K. Yoshino, Phys. Rev. Lett. **78**, 4285 (1997).
- ¹⁴R.K. Meyer, M. Liess, R.E. Benner, W. Gellermann, Z.V. Vardeny, M. Ozaki, K. Yoshino, Y. Ding, and T.J. Barton, Proc. SPIE **3145**, 219 (1997).
- ¹⁵S. Abe, in *Relaxation in Polymers*, edited by T. Kobayashi (World Scientific, Singapore, 1993), p. 215; S. Abe, M. Schreiber, W.P. Su, and J. Yu, Phys. Rev. B **45**, 9432 (1992).
- ¹⁶S. Abe, in *Primary Photoexcitations in Conjugated Polymers: Molecular Exciton versus Semiconductor Band Model* (Ref. 4), pp. 115–128.
- ¹⁷D. Yaron and R. Silbey, Phys. Rev. B **45**, 11 655 (1992).
- ¹⁸S.N. Dixit, D. Guo, and S. Mazumdar, Phys. Rev. B **43**, 6781 (1991).
- ¹⁹D. Guo, S. Mazumdar, S.N. Dixit, F. Kajzar, F. Jarka, Y. Kawabe, and N. Peyghambarian, Phys. Rev. B **48**, 1433 (1993).
- ²⁰S. Mazumdar and F. Guo, J. Chem. Phys. **100**, 1665 (1994); F. Guo, D. Guo, and S. Mazumdar, Phys. Rev. B **49**, 10 102 (1994).
- ²¹F. Guo, M. Chandross, and S. Mazumdar, Phys. Rev. Lett. **74**, 2096 (1995).
- ²²P.C.M. McWilliams, G.W. Hayden, and Z.G. Soos, Phys. Rev. B **43**, 9777 (1991).
- ²³Z.G. Soos and R.G. Kepler, Phys. Rev. B **43**, 11 908 (1991); R.G. Kepler and Z.G. Soos, *ibid.* **43**, 12 530 (1991).
- ²⁴D. Beljonne, J. Cornil, Z. Shuai, J.L. Brédas, F. Rohlfling, D.D.C. Bradley, W.E. Torruellas, V. Ricci, and G.I. Stegeman, Phys. Rev. B **55**, 1505 (1997).
- ²⁵B.S. Hudson, B.E. Kohler, and K.S. Schulten, in *Excited States*, edited by E.C. Lim (Academic, New York, 1982), pp. 1–95.
- ²⁶D. Guo and S. Mazumdar, J. Chem. Phys. **97**, 2170 (1992).

- ²⁷P.C.M. McWilliams and Z.G. Soos, *J. Chem. Phys.* **97**, 2172 (1992).
- ²⁸S.R. White, *Phys. Rev. Lett.* **69**, 2863 (1992).
- ²⁹Z. Shuai, S.K. Pati, W.P. Su, J.L. Brédas, and S. Ramasesha, *Phys. Rev. B* **55**, 15 368 (1997); Z. Shuai *et al.*, *ibid.* **58**, 15 329 (1998).
- ³⁰M. Boman and R.J. Bursill, *Phys. Rev. B* **57**, 15 167 (1998).
- ³¹M. Chandross and J.C. Hicks (unpublished).
- ³²V.A. Shakin and S. Abe, *Phys. Rev. B* **50**, 4306 (1994).
- ³³F.B. Gallagher and S. Mazumdar, *Phys. Rev. B* **56**, 15 025 (1997).
- ³⁴S. Ramasesha and Z.G. Soos, *J. Chem. Phys.* **80**, 3278 (1984).
- ³⁵Z.G. Soos and S. Ramasesha, *Phys. Rev. B* **29**, 5410 (1984).
- ³⁶M. Chandross, Y. Shimoi, and S. Mazumdar, *Chem. Phys. Lett.* **280**, 85 (1997).
- ³⁷W.T. Simpson, *J. Am. Chem. Soc.* **73**, 5363 (1951).
- ³⁸V.M. Agranovich and M.D. Galanin, *Electronic Excitation Energy Transfer in Condensed Matter* (North-Holland, Amsterdam, 1982).
- ³⁹F. Spano, V.M. Agranovich, and S. Mukamel, *J. Chem. Phys.* **95**, 1400 (1991).
- ⁴⁰I. Egri, *J. Phys. C* **12**, 1843 (1979).
- ⁴¹D. Haarer, M.R. Philpott, and H. Morawitz, *J. Chem. Phys.* **63**, 5238 (1975); A. Brillante and M.R. Philpott, *ibid.* **72**, 4019 (1980).
- ⁴²I. Ohmine, M. Karplus, and K. Schulten, *J. Chem. Phys.* **68**, 2298 (1978).
- ⁴³K. Ishida, H. Aoki, and T. Chikyu, *Phys. Rev. B* **47**, 7594 (1993).
- ⁴⁴K. Ishida, H. Aoki, and T. Ogawa, *Phys. Rev. B* **52**, 8980 (1995).
- ⁴⁵F.B. Gallagher and F.C. Spano, *Phys. Rev. B* **53**, 3790 (1996).
- ⁴⁶D. Mukhopadhyay, G.W. Hayden, and Z.G. Soos, *Phys. Rev. B* **51**, 9476 (1995).
- ⁴⁷M.J. Rice and Yu.N. Gartstein, *Phys. Rev. Lett.* **73**, 2504 (1994); Yu.N. Gartstein, M.J. Rice, and E.M. Conwell, *Phys. Rev. B* **52**, 1683 (1995).
- ⁴⁸W. Barford and R.J. Bursill, *Chem. Phys. Lett.* **268**, 535 (1997).
- ⁴⁹K. Ohno, *Theor. Chim. Acta* **2**, 219 (1964).
- ⁵⁰S.R. Bondeson and Z.G. Soos, *J. Chem. Phys.* **71**, 3807 (1979), and references therein.
- ⁵¹S. Mazumdar and Z.G. Soos, *Phys. Rev. B* **23**, 2810 (1981).
- ⁵²K. Schulten, I. Ohmine, and M. Karplus, *J. Chem. Phys.* **64**, 4422 (1976).
- ⁵³P. Tavan and K. Schulten, *J. Chem. Phys.* **85**, 6502 (1986).
- ⁵⁴Z.G. Soos, S. Ramasesha, and D.S. Galvão, *Phys. Rev. Lett.* **71**, 1609 (1993).
- ⁵⁵T. Hasegawa, Y. Iwasa, H. Sunamura, T. Koda, Y. Tokura, H. Tachibana, M. Matsumoto, and S. Abe, *Phys. Rev. Lett.* **69**, 668 (1992).
- ⁵⁶A. Chakrabarti, M. Chandross, and S. Mazumdar, *Proc. SPIE* **3145**, 424 (1997).
- ⁵⁷A. Chakrabarti and S. Mazumdar, following paper, *Phys. Rev. B* **59**, 4839 (1999).
- ⁵⁸Z. Shuai, J.L. Brédas, A. Saxena, and A.R. Bishop, *J. Chem. Phys.* **109**, 2549 (1998).